applied sciences

MDPI

Article

Fabrication of g-C_3N_4 Quantum Dots/$MnCO_3$ Nanocomposite on Carbon Cloth for Flexible Supercapacitor Electrode

Di Liu, Seung Hyun Hur, Jin Suk Chung and Won Mook Choi *

School of Chemical Engineering, University of Ulsan, 93 Daehak-ro Nam-gu, Ulsan 44610, Korea; ldygyx1020@gmail.com (D.L.); shhur@ulsan.ac.kr (S.H.H.); jschung@ulsan.ac.kr (J.S.C.)

* Correspondence: wmchoi98@ulsan.ac.kr; Tel.: +82-52-259-1065

Received: 16 October 2020; Accepted: 7 November 2020; Published: 9 November 2020

Abstract: In this study, the nanocomposite of g-C_3N_4 quantum dots/$MnCO_3$ on carbon cloth (q-MC//CC) is prepared via a simple hydrothermal method. The obtained q-MC//CC composite is employed for a flexible supercapacitor electrode. The g-C_3N_4 quantum dots could effectively improve the interface electrical conductivity and ion transportation of the $MnCO_3$ electrode, which results in superior electrochemical performance. The q-MC//CC electrode delivers a high specific capacity of 1001 F·g^{-1} at a current density of 1 A·g^{-1} and a good cycling performance of 96% capacity retention after 5000 cycles. Moreover, an asymmetric flexible supercapacitor (ASC) is assembled with q-MC//CC and carbon cloth as a positive and negative electrode, respectively, which exhibits a high energy density of 27.1 Wh·kg^{-1} at a power density of 500 W·kg^{-1}. In addition, the fabricated ASC device demonstrates the ability to power the light-emitting diode effectively under mechanical bending.

Keywords: $MnCO_3$; carbon cloth; g-C_3N_4 quantum dots; supercapacitors

1. Introduction

Supercapacitors have attracted considerable attention for the application of advanced energy storage devices of electronic vehicles and portable electronic devices due to their beneficial properties such as excellent power density, rapid charging time, and durability [1]. Electric double layer capacitors (EDLC) mainly use various carbon-based materials, such as activated carbon, carbon nanotubes (CNTs), and graphene. In EDLC, an accumulation of ionic charges occurs between the electrode and electrolyte of carbon-based electrodes, and carbon-based electrodes with large surface areas deliver high power density and long cycle stability. On the other hand, pseudocapacitors can exhibit substantially high specific capacitance and high energy density compared to EDLC, owing to the fast and reversible surface Faradaic redox reaction. In addition, transition metal oxide and carbonate materials have been explored as electrode materials of pseudocapacitors due to their high theoretical storage capacity and superior reversibility. Among them, Mn-based active materials have attracted a great deal of interest owing to the high theoretical capacitance, low cost, and natural abundance [2–5]. However, most research has been done with Mn-based oxides, and manganese carbonates ($MnCO_3$) are relatively new and popular active materials for pseudocapacitors. Recently, $MnCO_3$ has been extensively studied as a potential electrode of supercapacitors due to the low manganese valence state of +2 and the redox process to high manganese valence states (+3 or +4), which could show high electrochemical performance. The low manganese valence (+2) in $MnCO_3$ can exhibit a better hydroxyl ions insertion of alkaline electrolytes for the formation of $MnOHCO_3$ compared to high manganese valence states (+3 or +4) [5–7]. However, low electrical conductivity and poor cycle stability restrict the application of $MnCO_3$ as an active material in energy storage applications. To overcome these

drawbacks, an effective approach is to hybridize $MnCO_3$ using conductive carbon-based additives such as carbon [8], CNTs [9,10], and graphene [11–14], which have proved to be effective to improve electrochemical performance.

Graphitic carbon nitride (g-C_3N_4) recently attracted a lot of interest as a promising electrode candidate for electrochemical devices due to its high nitrogen content, good structural stability, and low interfacial impedance. Thus, g-C_3N_4 was employed in the transition metal oxides or hydroxide-based electrodes for supercapacitors. Chang et al. [15] synthesized novel sandwich-like MnO_2/g-C_3N_4 composites for supercapacitor electrodes and showed the enhanced electrochemical performance, which was ascribed to various active sites and the existence of N of g-C_3N_4 for better wettability with electrolytes. Gao et al. [16] reported the endurable supercapacitance using MnO_2/protonated g-C_3N_4. It showed that the strong hydrogen bonding between MnO_2 and the g-C_3N_4 can restrain particle agglomeration in the cycling test, resulting in stable energy storage performance. Ding et al. [17] fabricated the honeycomb nanostructured g-C_3N_4@$Ni(OH)_2$ for an asymmetric supercapacitor, where the g-C_3N_4 showed a good charge transport with good chemical stability. However, there are limited reports studying the application of g-C_3N_4 quantum dots (CNQDs) in energy storage fields.

Herein, we report a simple hydrothermal process to prepare the nanostructured $MnCO_3$ and CNQDs nanocomposites on carbon cloth (denoted as q-MC//CC). The active material of $MnCO_3$ and CNQDs nanocomposites is synthesized directly on the carbon cloth as a flexible conductive substrate, which is then also used for an electrode of a solid-state flexible asymmetric supercapacitor (ASC). $MnCO_3$ and CNQDs nanocomposites exhibit excellent electrochemical performance, including good specific capacitance and rate capability, which is attributed to the enhanced electrical conductivity and shorter ions pathway. Moreover, CNQDs have generally large surface areas and accessible edges that can function as active sites of electrochemical reaction, which would improve the electrochemical performance. The q-MC//CC electrode delivers a high specific capacitance of 1001.4 $F \cdot g^{-1}$ under a current density of 1 $A \cdot g^{-1}$ as well as good cycling performance (96% capacity retention). Furthermore, a solid-state binder-free flexible ASC using q-MC//CC electrode is demonstrated, showing a high energy density of 27.1 $Wh \cdot kg^{-1}$ at a power density of 500 $W \cdot kg^{-1}$ and good mechanical stability.

2. Materials and Methods

2.1. Preparation of g-C_3N_4 Quantum Dots

First, 5 g of melamine were calcinated in a muffle furnace at 550 °C for 4 h to obtain bulk g-C_3N_4. Then, 2 g of bulk g-C_3N_4 were treated in a mixture solution of sulfuric acid (40 mL) and nitric acid (40 mL) for about 2 h at room temperature. Then, the mixture was rinsed several times with deionized (DI) water, and the as-obtained white product was dispersed in the concentrated $NH_3 \cdot H_2O$. The mixture solution was transferred into a Teflon-lined stainless-steel autoclave with heating at 180 °C for 12 h. After the hydrothermal process, the precipitate was rinsed with DI water to remove residual NH_3 molecules. Subsequently, the treated g-C_3N_4 nanosheets were dispersed and sonicated in 100 mL water for 6 h, and the as-obtained aqueous suspension was centrifuged at 7000 rpm and dialyzed in a dialysis bag (3000 Da, Spectrum Lab. Inc) for 48 h to remove large particles. Finally, the CNQDs solution was obtained.

2.2. Synthesis of q-MC//CC Nanocomposites

First, carbon cloth was treated by immersing in a mixture acid solution (H_2SO_4:HNO_3 = 1:3) at room temperature for 24 h and then washed with DI water. For the typical synthesis of q-MC//CC nanocomposites (Figure 1), $MnSO_4 \cdot H_2O$ (3.38 g) was dissolved in DI water (134 mL), and NH_4F (0.6 g) was added to the above solution with stirring to form a transparent solution. After several minutes, urea (2.4 g) and 5 mg of CNQDs was added to the above homogeneous solution with 30 min stirring at room temperature. Then, the treated carbon cloth (3 × 1 cm^2) was immersed into the mixture solution and treated with the hydrothermal process, maintaining at 120 °C for 4 h. The obtained q-MC//CC

nanocomposites were washed with DI water to remove the residual reactants and dried at 60 °C. As a control sample, the $MnCO_3$ on carbon cloth sample was also synthesized by following the same procedure without adding CNQDs (denoted as MC//CC).

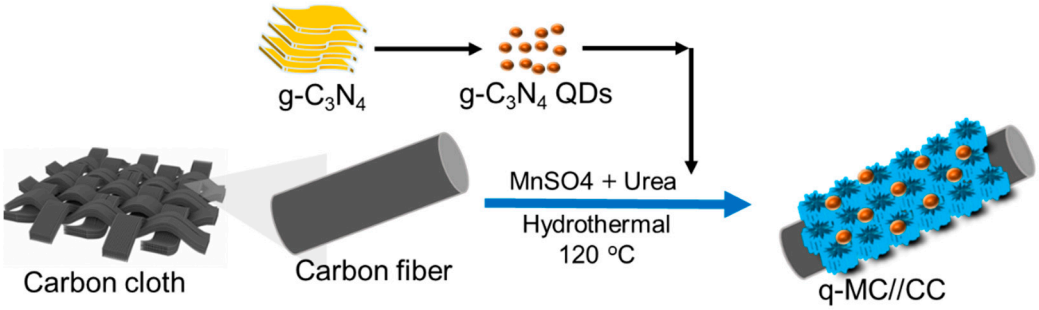

Figure 1. Scheme for the synthesis of g-C_3N_4 quantum dots/manganese carbonates ($MnCO_3$) nanocomposite on carbon cloth.

2.3. Characterization

A transmission electron microscope (TEM, H-8100, Hitachi, Tokyo, Japan) and a field-emission scanning electron microscope (FE-SEM, JEOL-JSM820, JEOL Ltd., Akishima-shi, Japan) were used to investigate the morphology of the obtained samples. X-ray photoelectron spectroscopy (XPS, K-alpha, Thermo Fisher, Waltham, MA, USA) measurements were carried out using monochromatic AlKα radiation (hν = 1486.6 eV). Contact angle measurements with electrolyte (1.0 M Na_2SO_4) droplets were performed to investigate the wettability of the q-MC//CC electrode using an Attension Theta Optical Tensiometer (Biolin Scientific AB, Stockholm, Sweden). Fourier transform infrared (FTIR) spectra were collected using a Nicolet IR 200 FT-IR spectrometer (Thermo Scientific, Waltham, MA, USA), and Raman spectroscopy (DXR Raman spectrometer, Thermo Scientific, Madison, WI, USA) was performed with a 532 nm excitation source.

2.4. Electrochemical Measurements

Electrochemical performance was investigated by a cyclic voltammetry (CV) test, galvanostatic charge/discharge (GCD) test, and electrochemical impedance spectroscopy (EIS) test. All electrochemical characterizations were carried out using a BioLogic VSP electrochemical workstation at room temperature. A three-electrode system was used to test the electrochemical performance of the prepared electrodes with platinum wire as a counter electrode and Ag/AgCl electrodes as a reference electrode. The obtained products such as MC//CC and q-MC//CC are used as a binder-free working electrode. The mass loading of active materials was about 2.5 mg in this work. All electrochemical characterizations were measured in an aqueous electrolyte of 1 M Na_2SO_4 at room temperature. EIS was performed at open circuit potential in a frequency range from 10 to 0.01 Hz with an AC amplitude of 5 mV. The solid-state flexible ASC was prepared using the q-MC//CC as a positive electrode and carbon cloth as a negative electrode, which were assembled with polyvinyl alcohol (PVA)/Na_2SO_4 gel electrolyte and a separator. The prepared two electrodes were wetted with the PVA/Na_2SO_4 gel electrolyte for 10 min and then assembled face to face with a separator. The specific capacitance (Cs) was calculated from the CV curves and galvanostatic charge–discharge curves using the following equations, respectively:

$$C_s = \frac{\int I(V)\,dV}{v \times m \times \Delta V}$$

$$Cs = \frac{I \times \Delta t}{m \times \Delta V}$$

where $\int I(V)\,dV$ is the area enclosed by the CV curves, ΔV (V) is the potential window, m (g) is the mass of electrode, v (mV s^{-1}) is the potential scan rate, and Δt (s) is the discharge time.

3. Results and Discussion

Figure 2a,b show FE-SEM images of as-prepared q-MC//CC nanocomposites. The pristine carbon cloth shows a smooth surface consisting of aligned carbon fiber bundles. After the hydrothermal reaction of the synthesis of q-MC//CC, it is observed that clusters of spindle-shaped petals of $MnCO_3$ were densely grown on the surface of carbon fibers. In addition, the prepared q-MC//CC sample shows good flexibility, as shown in the inset of Figure 2a. The morphology of MC//CC (Figure S1) has a similar nanostructure to that of q-MC//CC, showing that the addition of CNQDs has no effect on the morphological formation of $MnCO_3$. The TEM image (Figure 2c) of the q-MC//CC confirms that the CNQDs are uniformly embedded in $MnCO_3$, and the lattice fringe of CNQDs is found in the high resolution TEM (HRTEM) image (Figure 2d), where a lattice distance is 0.336 nm, corresponding to the (002) planes of g-C_3N_4. The SEM image of q-MC//CC and its elemental mapping from energy-dispersive X-ray spectroscopy (EDS) reveal the existence of the expected atomic elements (Figure 2e), which clearly confirms that Mn, C, and N elements are uniformly distributed on the $MnCO_3$ surface and the successful formation of q-MC//CC nanocomposite. In addition, the obtained q-MC//CC has a larger surface area (182 m^2/g) than the pristine carbon cloth (69 m^2/g) due to its unique nanostructure (Figure S2).

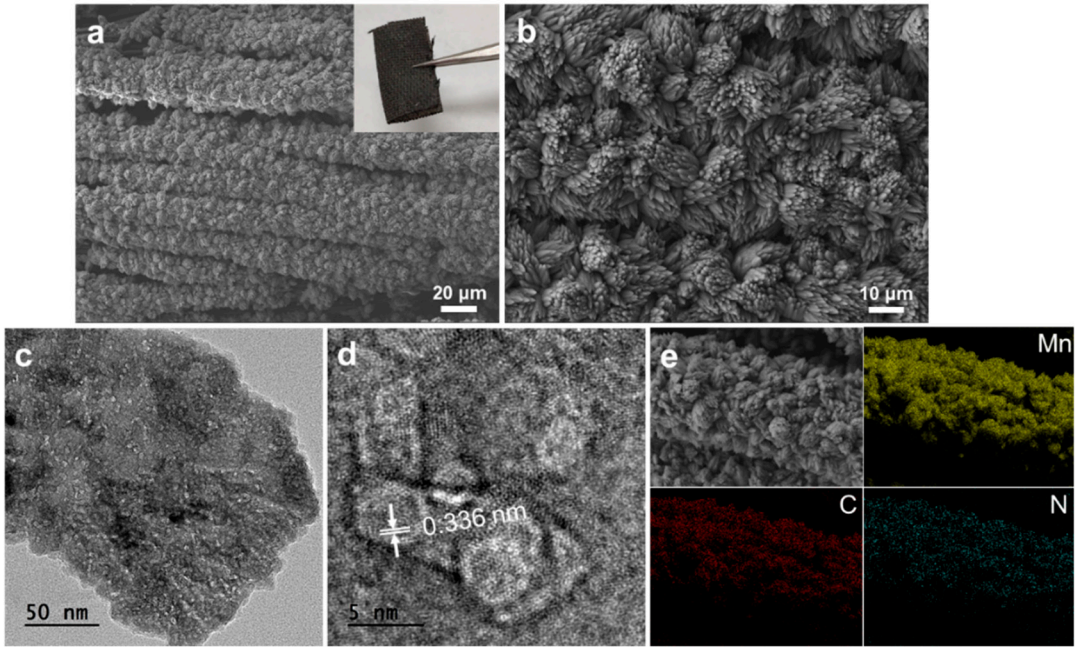

Figure 2. (**a**,**b**) SEM images of g-C_3N_4 quantum dots/$MnCO_3$ on carbon cloth (q-MC//CC). (**c**) TEM image of q-MC//CC and (**d**) High resolution TEM (HRTEM) image. (**e**) Energy-dispersive X-ray spectroscopy (EDS) mapping images of q-MC//CC.

An XPS study was performed to characterize the chemical compositions of the q-MC//CC. The XPS survey scans in Figure 3a show that both q-MC//CC and MC//CC samples contain the Mn, O, and C atoms, while the N peak is only found in the q-MC//CC nanocomposites due to CNQDs. The deconvolution of the Mn 2p spectrum of q-MC//CC (Figure 3b) displays two peaks located at 655.8 eV and 643.8 eV respectively, assigning to Mn $2p_{1/2}$ and Mn $2p_{3/2}$ with an energy separation of 12.0 eV, which coincides with Mn^{2+} [18,19]. In the high-resolution C1s spectrum of q-MC//CC (Figure 3c) and MC//CC (Figure S3), two typical peaks of the C-C bond at 284.6 eV and C=O bond at 288.5 eV are observed, relating to the surface carbon of the carbon cloth and carbon element in carbonate ions [20]. In addition, two additional peaks at 286.0 and 292.7 eV are only observed for q-MC//CC, which correspond to the C-N bond and carboxylate bond of CNQDs, respectively.

In addition, the high-resolution N 1s spectrum of q-MC//CC can be fitted into three peaks, as shown in Figure 3d, corresponding to =N- (398.4 eV), C=N-C (399.1 eV), and N-$(C)_3$ (400.4 eV) [21], indicating the presence of CNQDs in the q-MC//CC nanocomposite. The contact angle measurements with 1 M Na_2SO_4 electrolyte were performed to study the effect of CNQDs on the surface wettability of the prepared q-MC//CC composite. Figure S4 illustrates the images of electrolyte droplets on the prepared MC//CC and q-MC//CC composites, respectively. The q-MC//CC composite shows a lower contact angle with Na_2SO_4 electrolyte than MC//CC, which is due to the more ion-accessible surfaces by CNQDs. This enhanced surface wettability of the q-MC//CC composite facilitates the accessibility of electrolyte, leading to better electrochemical performance compared to the MC//CC composite. In addition, the FTIR spectra of the as-prepared q-MC//CC and MC//CC are shown in Figure S5. The characteristic peak of the Mn-O-Mn bond is observed at 727 cm^{-1} for both samples, while that of the characteristic peaks corresponding to the C-N (1033 cm^{-1}) and C=N bonds (1780cm^{-1}) are only found for q-MC//CC due to the existence of CNQDs.

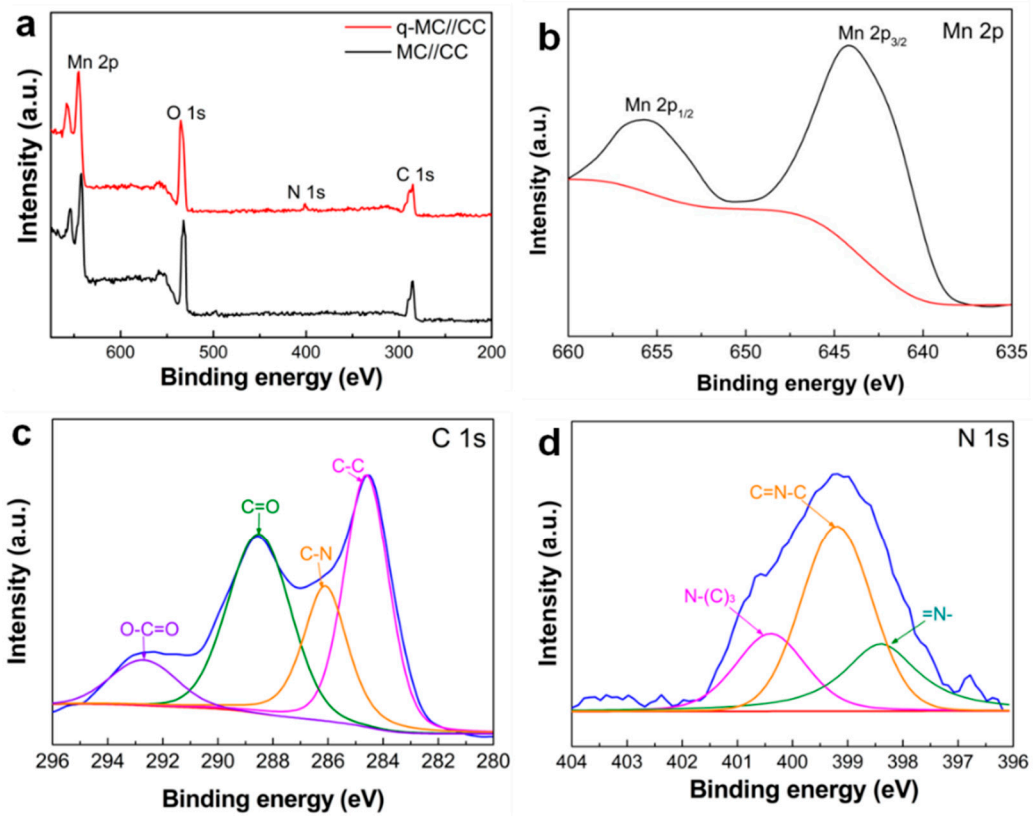

Figure 3. (**a**) XPS full survey scan of q-MC//CC and MC//CC. (**b**–**d**) High-resolution XPS of Mn 2p, C 1s, and N 1s of q-MC//CC, respectively.

The electrochemical performances of q-MC//CC composites as binder-free electrodes of supercapacitors are studied using CV and GCD characterization in 1 M Na_2SO_4 aqueous electrolyte using a three-electrode system. Figure 4a shows the CV curves of q-MC//CC and MC//CC measured at a scan rate of 5 $mV{\cdot}s^{-1}$ with potentials ranging from −0.2 to 0.8 V. CV curves of both electrodes show rectangular shapes in a potential window, indicating excellent capacitive behavior. The larger integral area of the CV curve for q-MC//CC electrode suggests higher specific capacitance than the MC//CC electrode, which represents its superior electrochemical property due to the synergistic effects of CNQDs and $MnCO_3$. The CV curves of q-MC//CC measured at different scan rates from 5 $mV{\cdot}s^{-1}$ to 100 $mV{\cdot}s^{-1}$ are shown in Figure 4b. The CV curve shapes are maintained upon increasing the scan rate, revealing fast ionic and electronic transportation. The current response also simultaneously increases along with the scan rate, showing a diffusion-controlled phenomenon. The GCD measurement of

the q-MC//CC electrode was performed at different current density (Figure 4c). All GCD curves show some linear and symmetric behavior, indicating capacitive characteristics and good reversibility of the q-MC//CC electrode. In addition, a noticeable potential drop at the discharge plot is not observed, suggesting the low internal resistance of the q-MC//CC electrode. The specific capacitance decreases with increasing current densities, due to slow ionic diffusion at high current. Figure 4d compares the calculated specific capacitance of q-MC//CC and MC//CC electrodes at current densities. It demonstrates the superior capacitive performance of q-MC//CC compared to the MC//CC electrode by the incorporation of CNQDs. The calculated specific capacitances of the q-MC//CC electrode are 1001.4, 609.3, 469.8, and 322.6 $F \cdot g^{-1}$ at 1, 2, 3, and 5 $A \cdot g^{-1}$, respectively. The charge storage mechanism of $MnCO_3$ involves the intercalation/de-intercalation of Na^+ with the redox reactions of the Mn ions. In addition, a surface process of the adsorption/desorption of Na^+ ions occurs. The redox reaction of Mn (II) ↔ Mn (I) occurs in Na_2SO_4 electrolyte: $MnCO_3 + Na^+ + e^- \leftrightarrow NaMnCO_3$. CNQDs on $MnCO_3$ can facilitate the intercalation/de-intercalation of Na+ ions and the redox reaction of Mn ions. This excellent electrochemical performance of the q-MC//CC electrode is highly comparable with previously reported $MnCO_3$-based electrodes (Table S1).

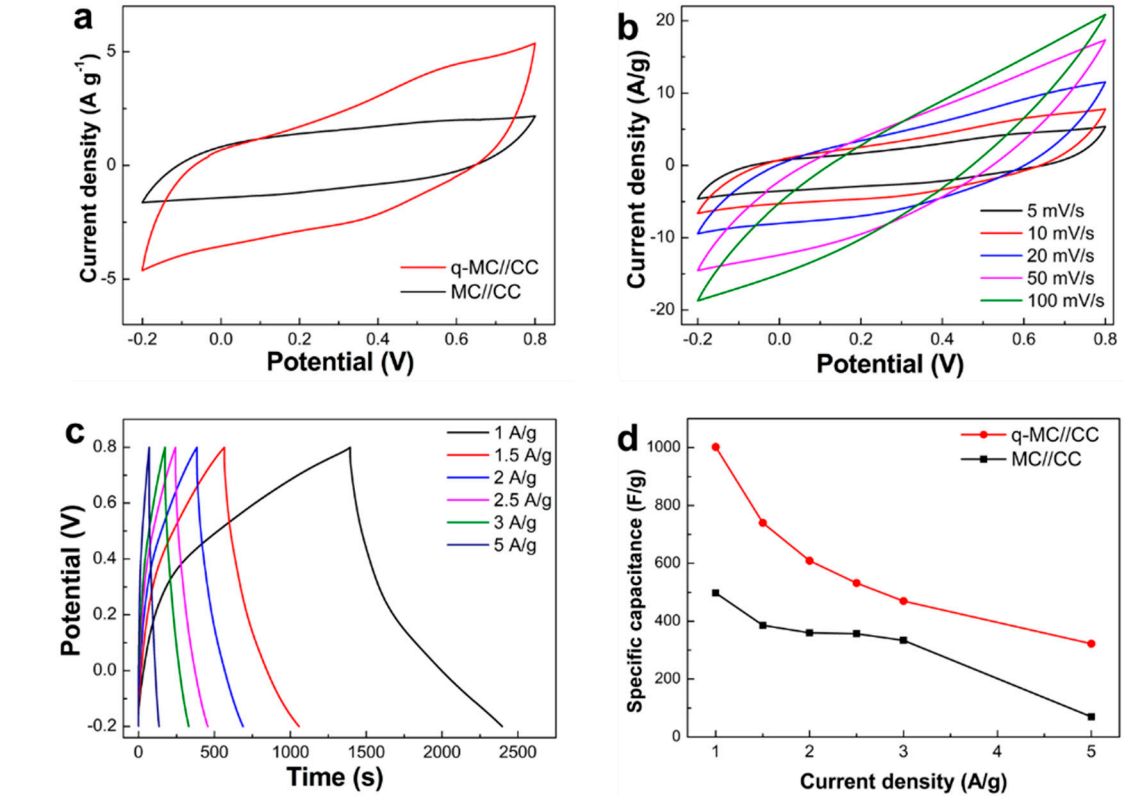

Figure 4. (**a**) Cyclic voltammetry (CV) curves of q-MC//CC and MC//CC. (**b**) CV curves of q-MC//CC at different scan rates. (**c**) Galvanostatic charge–discharge curves of q-MC//CC at different current densities. (**d**) Gavimetric specific capacitance of q-MC//CC at different current densities.

To further investigate the kinetics of ion and charge transfer, an EIS test was performed, and the Nyquist plots of q-MC//CC and MC//CC are presented in Figure 5a. The plots consist of a depressed circle at the high-frequency region and a straight line at the low-frequency region. The depressed is attributed to the charge transfer process of the Faradaic reaction at the interface of the electrode and electrolyte, and it belongs to the kinetic control, while the low-frequency region belongs to the mass transfer control. The formation of a depressed circle due to the roughness of the electrode/electrolyte surface results in the change of capacitance in double layer. In addition, the high slope of observed straight lines at the low-frequency region represents a small Warburg resistance. At the low-frequency

region, the linear shape suggests the fast ion diffusion in electrolyte and the adsorption process at the electrode surface. The solution resistances (Rs) of q-MC//CC and MC//CC are 2.1 Ω and 2.5 Ω; the as-prepared q-MC//CC enhances electron transport from electrode to current collector, implying the decrease in equivalent series resistance by the strong synergistic effect between $MnCO_3$ and CNQDs. The diameter of the depressed circle denotes the charge transfer resistance (R_{ct}). The q-MC//CC electrode exhibits a much lower R_{ct} value (10.8 Ω) than the MC//CC electrode (18.0 Ω), clearly revealing that the highly conductive interface between CNQDs and $MnCO_3$ significantly improves the charge transfer kinetics. The long-term cycle stability of q-MC//CC and MC//CC electrodes was examined by CV measurement for 5000 cycles at a scan rate of 50 $mV{\cdot}s^{-1}$. As shown in Figure 5b, the q-MC//CC electrode exhibits superior cycle performance with a 96% retention of its initial specific capacitance compared to the MC//CC electrode (71%). These results may be attributed to the distribution of CNQDs on $MnCO_3$, which can suppress the deformation and damage of the structure. As shown in the insert images in Figure 5b, the q-MC//CC electrode retains its initial microstructure after cycling, while the MC//CC electrode shows a swollen structure, revealing the excellent cycle stability of the q-MC//CC electrode.

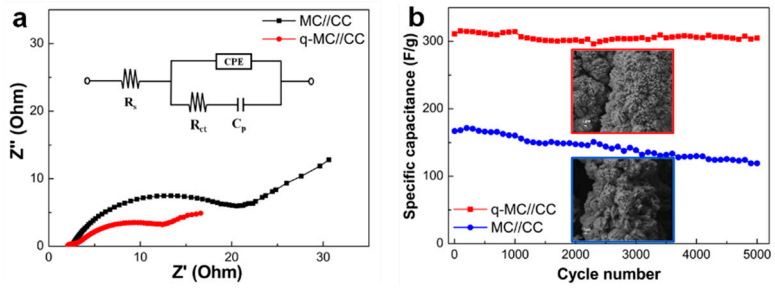

Figure 5. (**a**) Nyquist plots and (**b**) Cycling test of q-MC//CC and MC//CC along 5000 cycles at the scan rate of 50 $mV{\cdot}s^{-1}$ (insets show their SEM images after cycle test).

To study the practical application of q-MC//CC as a binder-free electrode, an all-solid-state asymmetric supercapacitor (ASC) device was constructed. The q-MC//CC electrode was the positive electrode and a carbon cloth was the negative electrode, which were then assembled with a polyvinyl alcohol (PVA)/Na_2SO_4 gel electrolyte and separator (Figure 6a). The CV curves measured at different scan rates are shown in Figure 6b. All CV curves present typical quasi-rectangular shapes without any obvious redox peaks, indicating the ideal capacitive behavior of the prepared ASC with the q-MC//CC electrode. Figure 6c presents the GCD curves at different current densities from 1 to 5 $A{\cdot}g^{-1}$. The nearly symmetric charge–discharge curves imply the high reversibility of the q-MC//CC electrode. The specific capacitances of ASC using the q-MC//CC electrode obtained from the curves are 195, 168, 147, and 130 $F{\cdot}g^{-1}$ at current densities of 1, 2, 3, and 5 $A{\cdot}g^{-1}$, respectively. The energy density of the assembled ASC is calculated and compared with other previous Mn-based ASC devices in the Ragone plot, as shown in Figure 6d. The prepared q-MC//CC electrode ASC delivers an energy density of 27.1 $Wh{\cdot}kg^{-1}$ at a power density of 500 $W{\cdot}kg^{-1}$ and retains 18.1 $Wh{\cdot}kg^{-1}$ even at a high power density of 2500 $W{\cdot}kg^{-1}$, which is superior to other systems reported [22–27]. To explore mechanical stability, the CV curves of the all-solid-state ASC using q-MC//CC are measured under different bending angles at a scan rate of 50 $mV{\cdot}s^{-1}$. The results in Figure 6e reveal that the CV curve shapes are well maintained with no remarkable changes, even at a bending angle of 180°, which reveals the good mechanical stability of the a-MC//CC electrode during bending. In addition, the application potential of the assembled ASC is further explored. Figure 6f shows that the ASC device under a flat and folded state lights up the green light-emitting diode (LED).

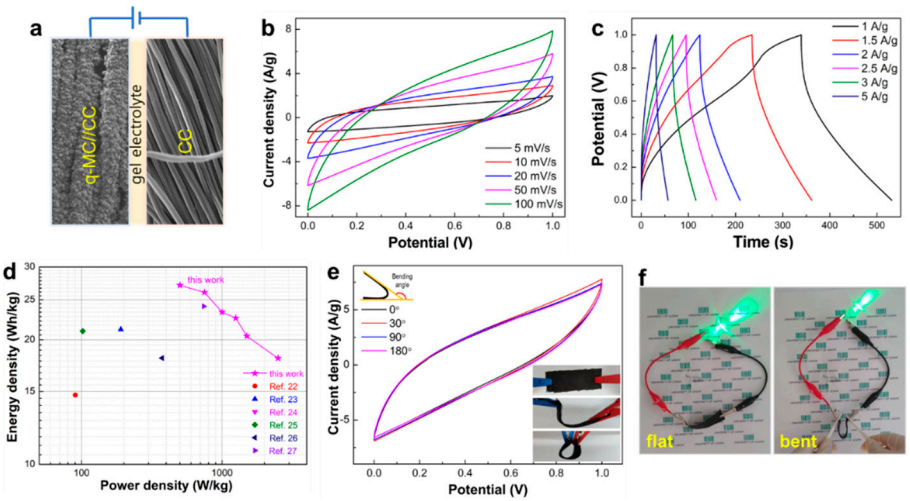

Figure 6. (**a**) Schematic illustration of assembly of all-solid-state asymmetric flexible supercapacitor (ASC). (**b**) Cyclic voltammetry (CV) curves at different scan rates and (**c**) galvanostatic charge–discharge curves at different current densities of ASC devices. (**d**) The Ragone plots of ASC devices and reported Mn-based supercapacitors. (**e**) CV curves of the ASC under mechanical bending. (**f**) Photo image of lighting LED (light-emitting diode) powered by ASC devices under flat and bent state.

4. Conclusions

In summary, q-MC//CC for a binder-free electrode of supercapacitor was successfully prepared via a simple hydrothermal method. The synergistic effects of CNQDs embedded on $MnCO_3$ can improve the interface electrical conductivity and shorten the ion diffusion paths for the utilization of $MnCO_3$. The binder-free q-MC//CC electrode shows enhanced supercapacitive performance, including a high specific capacitance of 1001.4 $F{\cdot}g^{-1}$ at a current density 1 $A{\cdot}g^{-1}$ and a superior cycling performance of 96% retention after 5000 cycles. In addition, the q-MC//CC electrode-based ASC was assembled with a gel electrolyte, which exhibited a high energy density of 27.1 $Wh{\cdot}kg^{-1}$ with a power density of 500 $W{\cdot}kg^{-1}$ with good mechanical stability. These results provide a promising alternative method to prepare a binder-free electrode for high-performance flexible supercapacitors.

Supplementary Materials: The following are available online at http://www.mdpi.com/2076-3417/10/21/7927/s1, Figure S1: SEM images of as-synthesized MC//CC, Figure S2. N_2 adsorption/desorption isotherms for CC and q-MC//CC composite, Figure S3. High resolution C 1s XPS spectrum of MC//CC, Figure S4. Image of the contact angle measurement of (a) MC//CC and (b) q-MC//CC with 1M Na_2SO_4 electrolyte, Figure S5. FT-IR spectrum for q-MC//CC and MC//CC, Table S1. Comparison of the electrochemical performance of q-MC//CC with previous reports.

Author Contributions: This research study was carried out as a collaboration of the aforementioned authors and was supervised by W.M.C.; D.L. initiated the idea and planned the experiments; J.S.C. and S.H.H. helped in data analysis; D.L. wrote the manuscript, which was edited by W.M.C. All authors have read and agreed to the published version of the manuscript.

Funding: This work was supported by the 2020 Research Fund of the University of Ulsan.

Conflicts of Interest: The authors declare no conflict of interest. The funders had no role in the design of the study; in the collection, analyses, or interpretation of data; in the writing of the manuscript, or in the decision to publish the results.

References

1. Wang, G.; Zhang, L.; Zhang, J. A review of electrode materials for electrochemical supercapacitors. *Chem. Soc. Rev.* **2012**, *41*, 797–828. [CrossRef]
2. He, S.; Hu, C.; Hou, H.; Chen, W. Ultrathin nanosheets supported on cellulose based carbon papers for high-power supercapacitors. *J. Power Sources* **2014**, *246*, 754–761. [CrossRef]

3. Gomez, J.; Kalu, E.E. High-performance binder-free Co-Mn composite oxide supercapacitor electrode. *J. Power Sources* **2013**, *230*, 218–224. [CrossRef]
4. Wu, Y.; Liu, S.; Wang, H.; Wang, H.; Zhang, X.; Jin, G. A novel solvothermal synthesis of Mn_3O_4/graphene composites for supercapacitors. *Electrochim. Acta* **2013**, *90*, 210–218. [CrossRef]
5. Devaraj, S.; Liu, H.Y.; Balaya, P. $MnCO_3$: A novel electrode material for supercapacitors. *J. Mater. Chem. A* **2014**, *2*, 4276–4281. [CrossRef]
6. Wang, L.; Sun, Y.; Zeng, S.; Cui, C.; Li, H.; Xu, H.; Wang, H. Study on the morphology-controlled synthesis of $MnCO_3$ materials and their enhanced electrochemical performance for lithium ion batteries. *CrystEngComm* **2016**, *18*, 8072–8079. [CrossRef]
7. Vardhan, P.V.; Sridhar, S.; Sivakkumar, S.R.; Mudali, U.K.; Devaraj, S. Facile synthesis of mesoporous $MnCO_3$ for supercapacitor applications. *J. Nanosci. Nanotechnol.* **2018**, *18*, 2775–2780. [CrossRef]
8. Wang, R.; Ma, Y.; Wang, H.; Key, J.; Brett, D.; Ji, S.; Shibin, Y.; Shen, P.K. A cost effective, highly porous, manganese oxide/carbon supercapacitor material with high rate capability. *J. Mater. Chem. A* **2016**, *4*, 5390–5394. [CrossRef]
9. Wen, Q.; Zhang, S.; Sun, M.; Jin, R. Fabrication of $MnFe_2O_4$ and $MnCO_3$ nanoparticles anchored on amorphous carbon-coated carbon nanotubes for high-performance lithium batteries and supercapacitors. *Nano* **2018**, *13*, 1850050. [CrossRef]
10. Wu, S.; Liu, C.; Dinh, D.A.; Hui, K.S.; Hui, K.N.; Yun, J.M.; Kim, K.H. Three-dimensional self-standing and conductive $MnCO_3$@Graphene/CNT networks for flexible asymmetric supercapacitors. *ACS Sustain. Chem. Eng.* **2019**, *7*, 9763–9770. [CrossRef]
11. Ghosh, D.; Giri, S.; Dhibar, S.; Kumar, C. Reduced graphene oxide/manganese carbonate hybrid composite: High performance supercapacitor electrode material. *Electrochem. Acta* **2014**, *147*, 557–564. [CrossRef]
12. Yuan, J.; Zhu, J.; Bi, H.; Zhang, Z.; Chen, S.; Liang, S.; Wang, X. Self-assembled hydrothermal synthesis for producing a $MnCO_3$/graphene hydrogel composite and its electrochemical properties. *RSC Adv.* **2013**, *3*, 4400–4407. [CrossRef]
13. Zhou, L.; Kong, X.; Gao, M.; Lian, F.; Li, B.; Zhou, Z.; Cao, H. Hydrothermal fabrication of $MnCO_3$@rGO composite as an anode material for high-performance lithium ion batteries. *Inorg. Chem.* **2014**, *53*, 9228–9234. [CrossRef]
14. Zhong, Y.; Yang, M.; Zhou, X.; Luo, Y.; Wei, J.; Zhou, Z. Orderly packed anodes for high-power lithium-ion batteries with super-long cycle life: Rational design of $MnCO_3$/large-area graphene composites. *Adv. Mater.* **2015**, *27*, 806–812. [CrossRef] [PubMed]
15. Chang, X.; Zhai, X.; Sun, S.; Gu, D.; Dong, L.; Yin, Y.; Zhu, Y. MnO_2/g-C_3N_4 nanocomposite with highly enhanced supercapacitor performance. *Nanotechnology* **2017**, *28*, 135705. [CrossRef] [PubMed]
16. Shi, Y.; Gao, S.; Yuan, Y.; Liu, G.; Jin, R.; Wang, Q.; Lu, J. Rooting MnO_2 into protonated g-C_3N_4 by intermolecular hydrogen bonding for endurable supercapacitance. *Nano Energy* **2020**, *77*, 105153. [CrossRef]
17. Dong, B.; Li, M.; Chen, S.; Ding, D.; Wei, W.; Gao, G.; Ding, S. Formation of g-C_3N_4@$Ni(OH)_2$ honeycomb nanostructure and asymmetric supercapacitor with high energy and power density. *ACS Appl. Mater. Interfaces* **2017**, *9*, 17890–17896. [CrossRef]
18. Lee, S.H.; Kwon, Y.; Park, S.; Cho, M.; Lee, Y. Facile synthesis of $MnCO_3$ nanoparticles by supercritical CO_2 and their conversion to manganese oxide for supercapacitor electrode materials. *J. Mater. Sci.* **2015**, *50*, 5952–5959. [CrossRef]
19. Zhang, R.; Wang, D.; Qin, L.C.; Wen, G.; Pan, H.; Zhang, Y.; Huang, X. $MnCO_3$/Mn_3O_4/reduced graphene oxide ternary anode materials for lithium-ion batteries: Facile green synthesis and enhanced electrochemical performance. *J. Mater. Chem. A* **2017**, *5*, 17001–17011. [CrossRef]
20. Chandra Sekhar, S.; Nagaraju, G.; Yu, J.S. Ant-cave structured $MnCO_3$/Mn_3O_4 microcubes by biopolymer-assisted facile synthesis for high-performance pseudocapacitors. *Appl. Surf. Sci.* **2018**, *435*, 398–405. [CrossRef]
21. Chen, J.J.; Mao, Z.Y.; Zhang, L.X.; Wang, D.J.; Xu, R.; Bie, L.J.; Fahlman, B.D. Nitrogen-deficient graphitic carbon nitride with enhanced performance for lithium ion battery anodes. *ACS Nano* **2017**, *11*, 12650–12657. [CrossRef]
22. Tang, Y.; Chen, S.; Chen, T.; Guo, W.; Li, Y.; Mu, S.; Yu, S.; Zhao, Y.; Wen, F.; Gao, F. Synthesis of peanut-like hierarchical manganese carbonate microcrystals via magnetically driven self-assembly for high performance asymmetric supercapacitors. *J. Mater. Chem. A* **2017**, *5*, 3923–3931. [CrossRef]

23. Zhang, H.; Lin, L.; Wu, B.; Hu, N. Vertical carbon skeleton introduced three-dimensional MnO_2 nanostructured composite electrodes for high-performance asymmetric supercapacitors. *J. Power Sources* **2020**, *476*, 228527. [CrossRef]
24. Wang, H.; Fu, Q.; Pan, C. Green mass synthesis of graphene oxide and its MnO_2 composite for high performance supercapacitor. *Electrochim. Acta* **2019**, *312*, 11–21. [CrossRef]
25. Amutha, B.; Sathish, M. A2V asymmetric supercapacitor based on reduced graphene oxide-carbon nanofiber-manganese carbonate nanocomposite and reduced graphene oxide in aqueous solution. *J. Solid State Electrochem.* **2015**, *19*, 2311–2320. [CrossRef]
26. Karuppaiah, M.; Akilan, R.; Sakthivel, P.; Asaithambi, S.; Shankar, R.; Yuvakkumar, R.; Hayakawa, Y.; Ravi, G. Synthesis of self-assembled micro/nano structured manganese carbonate for high performance, long lifespan asymmetric supercapacitors and investigation of atomic-level intercalation properties of OH^- ions via first principle calculation. *J. Energy Storage* **2020**, *27*, 101138. [CrossRef]
27. Zhao, N.; Fan, H.; Zhang, M.; Ren, X.; Wang, C.; Peng, H.; Li, H.; Jiang, X.; Cao, X. Facile preparation of Ni-doped $MnCO_3$ materials with controlled morphology for high-performance supercapacitor electrodes. *Ceram. Int.* **2019**, *45*, 5266–5275. [CrossRef]